




Shepherd electron effects in multiple ionization of rubidium by circularly polarized intense laser fields

Shiwei Liu^{1,2}, Difa Ye^{1,3} [✉], Yuhai Jiang^{4,5} [✉] & Jie Liu^{6,7} [✉]

Nonsequential double/multiple ionization (NSDI/NSMI) of atoms in strong laser fields is a paradigm system for studying field-intervened electron-electron correlation. However, there exists a long-standing debated topic as to how NSDI/NSMI is triggered in a circularly-polarized laser field. In this contribution, it is shown counter-intuitively that the NSMI of alkali atoms is strongly enhanced due to a mechanism induced by their intrinsic shell structure, coined as the shepherd electron effect. Specifically, we find that the early-released outermost electron (the shepherd electron) can be stabilized on the Rydberg states even after dislodging some other inner-shell electrons and thus lead to the emergence of a transient hollow atom. Experimental signatures of the shepherd electron effect and its real-time observation with the attoclock technique are discussed. These results have substantially enriched our understanding of NSMI, beyond the well-accepted cascade recollision picture. They might have applications in coherent extreme-ultraviolet (XUV) light amplification.

¹Beijing Computational Science Research Center, 100193 Beijing, China. ²School of Science, Beijing University of Civil Engineering and Architecture, 100044 Beijing, China. ³Laboratory of Computational Physics, Institute of Applied Physics and Computational Mathematics, 100088 Beijing, China. ⁴Center for Transformative Science and School of Physical Science and Technology, ShanghaiTech University, 201210 Shanghai, China. ⁵Shanghai Advanced Research Institute, Chinese Academy of Sciences, 201210 Shanghai, China. ⁶Graduate School, China Academy of Engineering Physics, 100193 Beijing, China. ⁷HEDPS, Center for Applied Physics and Technology, and College of Engineering, Peking University, 100871 Beijing, China. ✉email: ye_difa@iapcm.ac.cn; jliu@giscaep.ac.cn

Strong-field ionization of atoms in circularly polarized (CP) or close-to-CP intense laser fields is of fundamental interest and has widespread applications in attoclock technique, in which the periodically spinning carrier of a CP field acts as the minute hand while the slowly varying pulse envelope can also serve as the hour hand, providing an ultrafast chronoscope for the ionization dynamics¹. Therefore, it is crucial to fully explore and understand the underlying physics which, however, is to some extent still puzzling. At high laser intensities where the electrons are expected to be deprived one by one, i.e. via the sequential ionization, the ionization time was found to deviate from the prediction of the widely accepted single-active-electron approximation². Even more appealing is the nonsequential double ionization (NSDI) which proceeds in three steps: a preliminarily released electron, subsequently driven back by the oscillating laser field, finally dislodges another electron^{3,4}. With the help of multi-particle coincidence detection techniques, exotic signatures of the field-intervened electron-electron (e - e) correlation^{5–7} or anti-correlation^{8,9} during the NSDI process have been revealed in experiment and the underlying mechanisms are subsequently explored by classical¹⁰, semiclassical^{11–13}, and quantum simulations^{14–17}.

Traditionally, it is believed that NSDI is more favorable in linearly polarized (LP) fields but would be significantly suppressed in CP fields because the released electron might spiral away from the parent ion due to a considerable drift momentum. This scenario was verified in some early experiments¹⁸ but not in others¹⁹, and thus had aroused a surge of debate during the past years^{20,21}. It was later realized that the initial tunneling momentum might compensate the drift momentum for the alkaline-earth atoms, based on which a phase diagram was predicted, indicating what kind of atoms under which laser parameters can NSDI take place^{22,23}.

Stepping forward to the nonsequential multiple ionization (NSMI), while most of the early experiments were performed with the rare-gas atoms (see, e.g., refs. 24–29), the combination of the laser cooling technique and the strong-field reaction microscope has offered the opportunity to extend the discussions to the family of alkali atoms recently. Up to now, however, only the

single^{30,31}, double³², and sequential multiple ionizations³³ have been explored. In this paper, we focus on the NSMI of alkali atoms under CP radiations and find an shepherd electron effect³⁴. We demonstrate our theory with the rubidium (Rb) atom that has versatile applications in precision measurements³⁵ and Bose-Einstein condensation³⁶, while the physical picture is general and can be extended to other species of atoms. The essential idea is that a CP field can be applied to successively strip several electrons, among which the rescattering of the inner-shell electrons are strongly suppressed while the outermost one (referred to as the shepherd electron thereafter) is stabilized on an elliptical orbit. This effectively produces a vacancy in the atom, therefore with the return of the shepherd electron some intriguing effects can be induced. First, the shepherd electron may further dislodge the inner-shell electrons by recollisions. Second, if no recollision occurs, it can be recaptured after some other inner-shell electrons are ionized as such the Coulomb focusing effect of the parent ion becomes stronger. As a result, we predict a double-knee structure on the ion yield curve that is universal from double to quintuple ionizations. The knee structure in the regime below the saturation (BS) intensity is related to recollision while the above-threshold (AS) one is attributed to frustrated multiple ionization. The latter also leaves footprints with a long tail (or a halo structure) on the recoiled-ion momentum spectrum and can be detected by the attoclock technique.

Results and discussion

Double-knee structure. Our study is facilitated by a classical trajectory Monte Carlo approach with Heisenberg potential (CTMC-H, see Methods), which well describes the multi-shell structure of alkali-metal atoms^{33,37,38}. The CTMC-H model has achieved great success in solving the ionization time puzzle in sequential double ionization of Ar³⁹, interpretation of the kinetic energy release (KER) spectrum of laser-driven dissociation of D_3^+ molecule⁴⁰, as well as quantitatively reproducing the ionization cross section in traditional atomic collisions⁴¹ and thus explaining the Wannier threshold law⁴² and spin polarization⁴³, to name only a few. As demonstrated in Fig. 1a, our classical atom highly resembles the shell structure of Rb, i.e., the outermost 5s electron

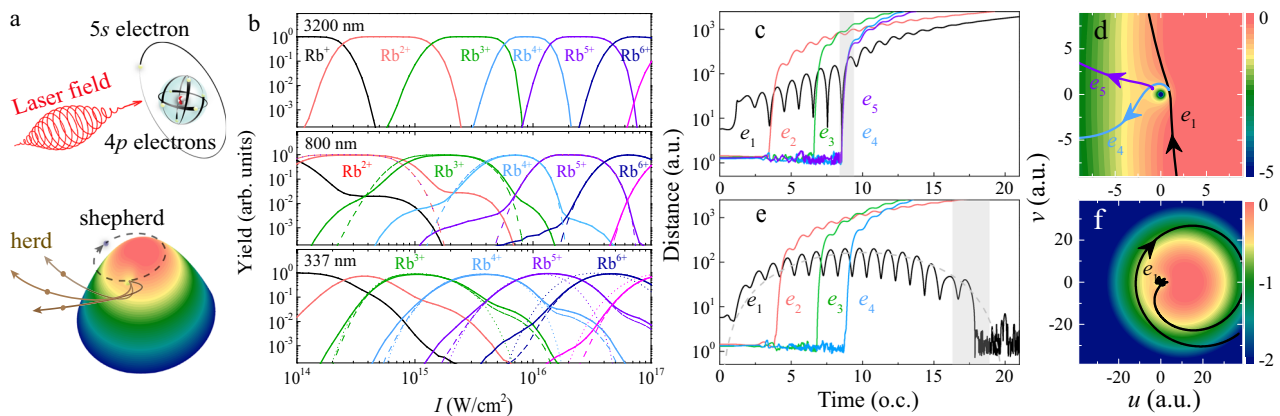


Fig. 1 Double-knee structure on the ion yield curve and the associated physical mechanisms. **a** Schematic illustration of a model Rb atom with seven active electrons irradiated by a circularly polarized laser field, manifesting the shepherd electron effect. **b** Ion yield of Rb^{n+} ($n = 1, 2, 3, \dots$) as a function of the peak laser intensity at three different laser wavelengths, i.e., $\lambda = 3200, 800,$ and 337 nm, respectively. Here, the results obtained by simulations with seven ($4p^6 5s^1$) active electrons (solid curves) are compared to that with only six ($4p^6$, dashed curves) or five ($4p^5$, dotted curves) active electrons. Such comparison disentangles the decisive role of the inter-shell and intra-shell e - e correlations. **c** A typical trajectory of quintuple ionization, in which the outermost shepherd (5s, black) electron is driven back and forth at the vicinity of the inner-shell electrons, dislodging the herd (4p electrons) either by soft [e_2 (red) and e_3 (green)] or hard [e_4 (blue) and e_5 (violet)] recollisions. The spacial configuration at the instant of the recollision [shaded area of (c)] is shown in (d), where the contour plot shows the effective potential Ω . **e** and **f** Demonstrate a typical trajectory of the frustrated quadruple ionization, in which, after the stripping of three 4p electrons, the 5s shepherd electron is recaptured by the parent ion during the ramp-off of the external laser field. The gray dashed line in (e) represents the adiabatic solution $r_0 = \sqrt{2\mathcal{E}_0 f(t)/\omega^2}$.

is much further from the nucleus than the other six $4p$ electrons which arrange pairwise around the nucleus and occupy the six corners of an octahedron. We exploit the CTMC-H model to simulate the multi-electron dynamics of the laser-driven Rb system. The laser electric field takes the form

$$\mathcal{E}(t) = \frac{\mathcal{E}_0 f(t)}{\sqrt{1 + \epsilon^2}} \left[\epsilon \sin(\omega t) \hat{e}_x - \cos(\omega t) \hat{e}_y \right], \quad (1)$$

with \mathcal{E}_0 , ω and ϵ denoting its amplitude, frequency, and ellipticity, respectively. The envelope function is given by $f(t) = \sin^2(\pi t/T)$ and T represents the full pulse duration. In our simulations, we consider a maximum of seven active electrons because the laser intensities are not strong enough to ionize the $4s$ -shell and other even more deeply bound electrons.

Figure 1b shows the ion yield of Rb^{n+} ($n = 1, 2, 3, \dots$) as a function of the peak laser intensity when the atom is irradiated by a CP field with a full pulse duration of twenty optical cycles. The results are compared at three different wavelengths. In the long-wavelength limit ($\lambda = 3200$ nm), it can be seen that each ion yield curve has the same tendency: a sharp ratchet-up followed by a plateau (saturation regime) and again a sharp drop-off. If the wavelength is decreased to $\lambda = 800$ nm, a universal double-knee structure appears for all the ionization channels, see the solid curves. The double-knee structure retains at $\lambda = 337$ nm and seems more asymmetric.

To reveal the possible physical mechanisms behind the sensitive wavelength-dependent ionization dynamics, we carry out two additional groups of simulations with only six ($6e$, $4p^6$) or five ($5e$, $4p^5$) active electrons and compare them with the full simulations with seven active electrons ($7e$, $4p^6 5s^1$). In the $6e$ model, we intentionally remove the outermost $5s$ electron and only consider the laser interaction with the remained six electrons. The $5e$ model is similar except that another $4p$ electron is also removed. As shown in Fig. 1b, the characteristic double-knee structure at 800 nm totally disappears in the $6e$ simulations (dashed curves). We thus infer that the outermost electron is responsible for the NSMI of all the inner-shell electrons, which is different from the rare-gas atoms, in which other channels such as the cascade NSMI are expected to dominate the ionization processes, i.e., the double, triple, and quadruple ionizations respectively induced by recollision of the firstly, secondly, and thirdly released electrons and so on⁴⁴. The situation becomes different at $\lambda = 337$ nm, for which the removal of the $5s$ electron strongly suppresses the knee-structure in the BS regime but does not change much of the reversed knee-structure in the AS regime. With the further removal of a $4p$ electron, the double-knee structure again totally disappears. This indicates that both the inter-shell and intra-shell electron correlations play indispensable roles in this case, therefore the correlated electron dynamics is more complicated.

Taking full advantage of the classical trajectory back-analysis²², we can achieve more insight into the underlying mechanisms, please refer to Fig. 1c–f for two types of typical trajectories. We first convert the system into the frame that rotates with the time-dependent CP field⁴⁵, following the transformation $u = x \sin \omega t - y \cos \omega t$, $v = x \cos \omega t + y \sin \omega t$, and $w = z$. In the rotating frame (u, v, w) , the laser field turns out to be an quasi-static electric field. Consequently, the converted system exhibits a conserved quantity $J = \dot{\sigma}^2/2 + \Omega$, which is known as Jacobi's integral. Here, $\dot{\sigma} = (\dot{u}, \dot{v}, \dot{w})$ represents the momentum of the electron in the rotating frame,

$$\Omega = -\frac{1}{r} - \frac{\omega^2 r^2}{2} + \frac{\mathcal{E}_0 u f(t)}{\sqrt{2}} \quad (2)$$

is the effective potential energy, and J imposes a constraint on the

permissible phase space for electron motion. By setting $\dot{\sigma} = 0$, an implicit definition of a surface is obtained, wherein the velocity is equal to zero. This surface is referred to as the zero-velocity surface or Hill surface. Figure 1 demonstrates the projection of the Hill surface onto the (u, v) plane through surface or contour plots, in which the parent ion is situated at the origin, creating a deep well around it and is encompassed by a region of higher potential. A maximum of the potential energy landscape can be found approximately at the position $(u = \mathcal{E}_0/\omega^2, v = 0)$, situated to the right of the parent ion. While at the left side, there exists a saddle point where electrons can cross over the Coulomb barrier.

In the rotating frame, we find that the shepherd electron adiabatically follows the $\Omega = 0$ surface. This gives rise to an estimation of the electron trajectory r_0 (gray dashed curve in Fig. 1e)

$$r_0 \approx \frac{\sqrt{2} \mathcal{E}_0 f(t)}{\omega^2}. \quad (3)$$

With the adiabatic ramp on and off of the laser field, the Hill surface firstly expands and then shrinks, and the shepherd electron is gradually pulled out and sent back again to the vicinity of the nucleus. The return of the shepherd electron can trigger two possible processes. First, it might recollide with the inner-shell electrons³ and lead to the NSMI as shown in Fig. 1c, d, which is responsible for the strong enhancement of the ion yield of Rb^{n+} ($n = 2, 3, 4, \dots$) as evidenced by the characteristic knee structures in the BS regime⁴⁶. Despite the shepherd electron has a negligible drift momentum since it is released during the onset of the laser pulse and therefore experiences a small vector potential, it is subsequently driven back and forth at the vicinity of the parent ion by the oscillating laser field and its kinetic energy upon recollision can reach up to $U_p = \mathcal{E}_0^2/4\omega^2$, the ponderomotive energy. Taking again the trajectory shown in Fig. 1c for example, the energy of the returning electron is about 200 eV (at $t \approx 8.5$ o.c., see Fig. 2a, b for the corresponding energy evolution), which provides a sufficient amount of energy for the ionization of several inner-shell electrons. Second, after the exfoliation of some inner-shell electrons, the Coulomb focusing effect⁴⁷ of the parent ion becomes much stronger than what the electron can experience at the very beginning of its leave. So the electron has a large probability to be recaptured by the parent ion, leading to the frustrated MI, see Fig. 1e, f. This is the dominant mechanism for the reversed knee structure in the AS regime. We have conducted a statistical analysis on the return time of the shepherd electron for the reversed knee. As illustrated in Fig. 2c, most of the shepherd electrons are recaptured during the last two or three laser cycles when the laser field is turned off. Here, we would like to note that the shepherd electron effect seems similar to but not a simple variation of the conventional frustrated tunnel ionization (FTI) process^{48,49}. For FTI, it has been shown in prior works that the recapture process takes place predominantly in linearly polarized light but vanishes for circularly polarized light; in contrast, the shepherd electron effect happens in circularly polarized light. It is due to ionization of the outermost electron in the rising edge of the pulse similar to the mechanism demonstrated in ref. 23, whereas the shepherd electron effect on NSMI was not revealed therein.

Hallow atom and the Attoclock signature. In addition to the double-knee structure on the ion-yield curve, the shepherd electron effect also leaves footprints on the ion momentum spectrum. Taking Rb^{3+} at $I = 5 \times 10^{15}$ W/cm² as an example, we plot the momentum distribution (P_x, P_y) in the polarization plane, as shown in Fig. 3. The momentum distribution displays a donut shape mainly consisting of two rings (Fig. 3a): one colored red

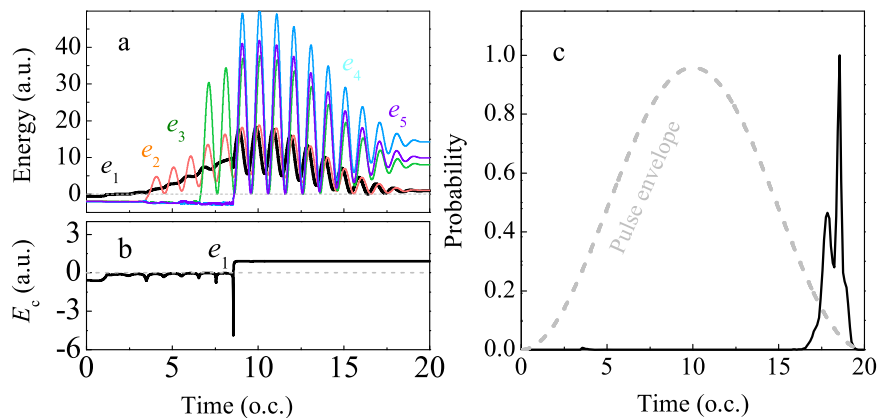


Fig. 2 Some temporal information of the shepherd electron. **a** Energy evolution of the electrons corresponding to the typical trajectory shown in Fig. 1c. **b** The compensated energy⁶⁶ as a function of time, which is negative for $t \leq 8.5$ o.c. so that one can say the shepherd electron remains in the excited state. **c** Time distribution of the shepherd electron when it is recaptured by the Rb^{4+} ion. The laser intensity is 5×10^{15} W/cm².

and centered close to the zero plus another concentric ring colored yellow with higher momentum³³. Besides, there also exist some scattered events beyond $P_r = \sqrt{P_x^2 + P_y^2} > 6$ a.u. This halo structure is not observed in the $6e$ simulations (Fig. 3b), again pointing to the pivotal role of the shepherd electron in producing the high-energy ion, which can be more clearly seen in the momentum distribution of P_r , as shown in Fig. 3c. Here, a double-hump structure, with one hump at $P_r \approx 1$ a.u. and the other one at $P_r \approx 5$ a.u. [corresponding to the inner and outer rings in the (P_x, P_y) distribution, respectively] can be found both in the $6e$ and $7e$ simulations. However, the momentum cuts off at $P_r \approx 6$ a.u. for the $6e$ simulations, but extends up to $P_r \approx 10$ a.u. for the $7e$ simulations.

The above results can be explained by the simple-man model associated with the over-barrier-ionization (SMOBI), in which the electrons are assumed to be released when the laser field reaches the OBI threshold. Therefore, the absolute value of their momenta can be estimated as $p_{en} = \mathcal{E}_n/\omega$, where $\mathcal{E}_n = I_{pn}^2/4n$ is the critical field strength leading to the OBI of the n -th electron, and I_{pn} is the n -th ionization energy of the Rb atom⁵⁰. Because the outermost electron can be easily ionized during the rising edge of the laser pulse, its momentum is extremely small and thus can be ignored. Therefore, the ion momentum of triple ionization mainly depends on the second and third ionized electrons: The inner ring structure results from the electrons ionized in the opposite direction ($P_r \approx p_{e3} - p_{e2}$), while the outer ring structure is caused by the electrons ionized in the same direction ($P_r \approx p_{e3} + p_{e2}$)⁵¹. This explains the first two humps in Fig. 3c, which are the common features of the $7e$ and $6e$ simulations. In contrast, we find that the long tail of Rb^{3+} momentum spectrum that is only observed in the $7e$ simulations seems to be contributed by three $4p$ ionized electrons, i.e., $P_r \approx p_{e2} + p_{e3} + p_{e4}$.

The remained question is how a triply ionized Rb atom acquires such a large energy and is related to the fourth electron? The answer lies in the typical trajectory of Fig. 1e, where after the subsequent ionization of the e_2 , e_3 , and e_4 , the shepherd electron is driven back to the origin when the laser field is ramped off and is recaptured by the Rb^{4+} to form an excited Rb^{3+*} ion, therefore the recoil ion momentum is equal to the sum of three $4p$ electrons' momenta. Due to the trapping of the outermost electron into the Rydberg states, the Rb^{3+*} ion has the same charge mass ratio with the Rb^{3+} ion and thus can not be distinguished from them, which accounts for the relatively slow decrease of the Rb^{3+} yields as compared with the results of the $6e$ model. This consolidates our findings on the pivotal role of the

shepherd electron as the dominant mechanism underlying the reversed knee structure.

Since the shepherd electron is pumped into and stabilized on an elliptical orbit even after the deprive of some inner-shell electrons (recall the dashed curve in Fig. 1e at $t > 10$ o.c.), this effectively produces a transient vacancy in the atom, similar to the hollow atom triggered by X-rays⁵². In the XUV case, a hollow atom can be produced only when the photoionization rate is comparable to or faster than the Auger decay rate. In our case, the efficiency is ensured by the long life time of the highly excited shepherd electron. Furthermore, for our hollow atom is produced by the absorption of multiple NIR photons, it might have applications in coherent XUV light amplification by means of high-order harmonic emission.

Real-time observation of the shepherd electron effect can be realized with the attoclock technique, in which the field envelope provides a hour hand for the coarse timing of the ionization, with a direct mapping of the momentum to the ionization time of the electrons². In Fig. 3d, we show the ionization time distributions of the triple ionization, which is constituted of three separated peaks representing the ionization sequence of the three ionized electrons. One might also notice that there exists a sub-peak (shaded areas) following each main peak. These side-band structures are related to those ions with high recoil momentum $P_r > 6$ a.u., for which the $5s$ electron is recaptured and the three sub-peaks indeed correspond to the ionization times of three $4p$ electrons.

As a double-check of the proposed mechanism, we have also calculated the ion momentum spectra at the other two different wavelengths, as shown in Fig. 3e, f, respectively. In the long-wavelength limit, the momentum spectra calculated with the $6e$ and $7e$ models are almost coincident and the corresponding halo structure totally vanishes, signifying the disappearance of the shepherd electron effect. On the other side, i.e., in the short-wavelength limit, the $7e$ calculation yields a momentum spectrum that can even extend to $P_r \approx p_{e3} + p_{e4} + p_{e5}$, which is significantly broader than the $6e$ calculation. Back-analysis of the classical trajectories shows that there is a small probability that both the e_1 and e_2 electrons are recaptured.

Phase diagram. After identifying the dominant mechanisms, below we make some analytical discussions to obtain a more general and intuitive picture, based on which a phase diagram will be presented, showing the parametric space that our predictions could be observable. For this purpose, we first assume that the field-driven ionizations most probably take place at the rising edge of the pulse envelope when the field amplitude reaches the

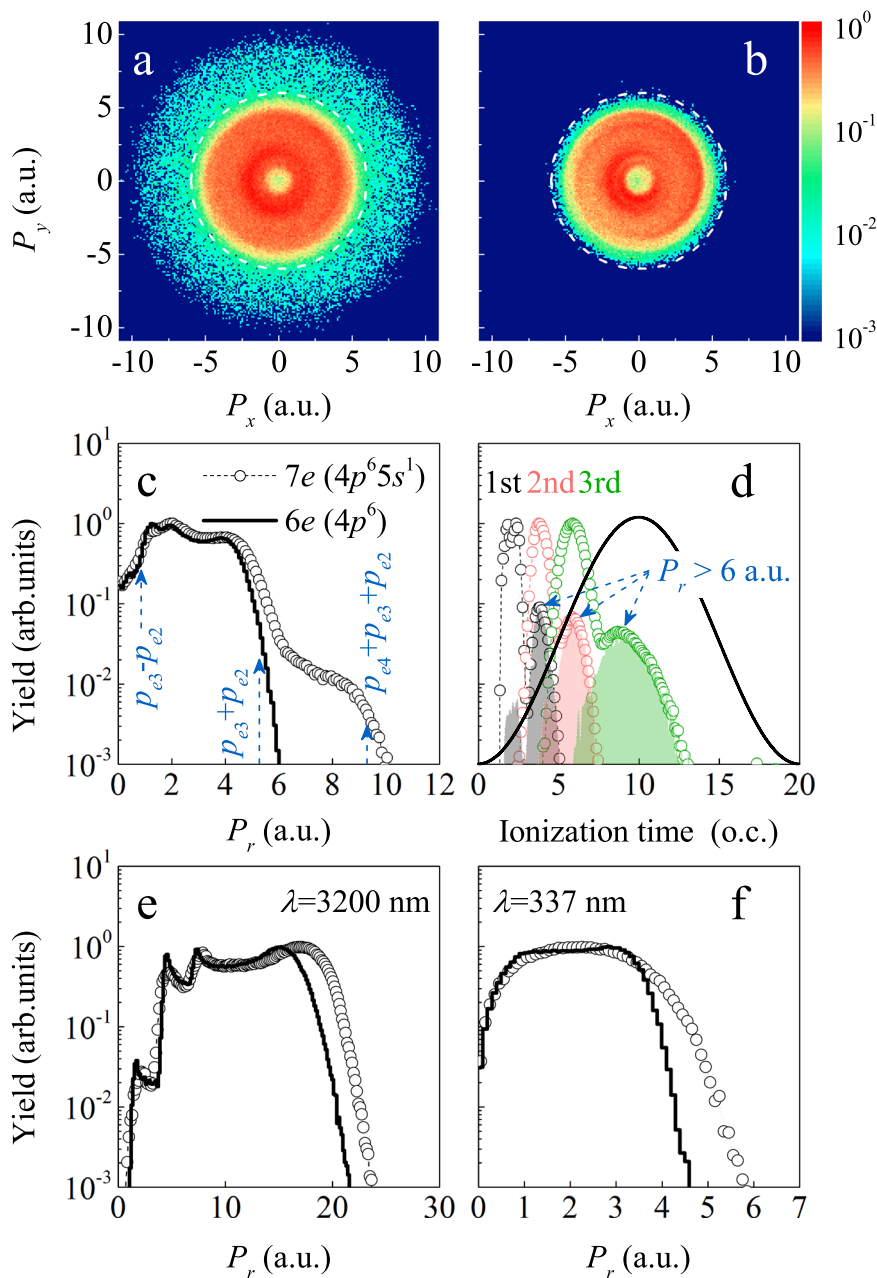


Fig. 3 Halo structure on the recoiled-ion momentum spectrum and the real-time observation with attoclock technique. The momentum distributions of Rb^{3+} in the polarization plane at the laser intensity of $5 \times 10^{15} \text{W/cm}^2$, as predicted by the (a) seven- ($4p^6 5s^1$) and (b) six- ($4p^6$ only) active-electron models, respectively. The laser wavelength λ is 800 nm. The dashed white circles correspond to $P_r = 6$ a.u. to guide the eyes. **c** Shows the distribution of $P_r = \sqrt{P_x^2 + P_y^2}$, where a long tail can be seen from the 7e simulation but absent in the 6e case. This is due to the frustrated multiple ionization, see text for details. **d** The ionization time distributions of the firstly (black), secondly (red), and thirdly (green) released electrons for the whole ensemble of Rb^{3+} (scatters), in comparison with those events that end up with high-ion-momentum $P_r > 6$ a.u. (shaded areas). **e, f** The same as (c), but for different laser wavelengths.

OBI threshold and the corresponding electrons are released at the local maximum (along the major axis) of an elliptically polarized (EP) laser field, as demonstrated in Fig. 4a. At this time, the field amplitudes along the major and minor axes are $\mathcal{E}_{y0} = I_{pn}^2/4n$ and $\mathcal{E}_{x0} = \epsilon\mathcal{E}_{y0}$, respectively. We want to examine if these field-released electrons can be driven back to the parent ion to induce the shepherd electron effects. In the classical scenario, the ionized electron has a random initial transverse (perpendicular to the major axis) momentum that obeys the Gaussian distribution $W(p_{\perp}) \propto \exp[-\sqrt{2}I_{pn}p_{\perp}^2/\mathcal{E}_{y0}]^{53}$; if the initial transverse momentum is able to compensate the drift momentum imposed by the

laser field, i.e., $p_{\text{drift}} = \mathcal{E}_{x0}/\omega$, then the ionized electron has a considerable probability to return to the vicinity of parent ion. In our following calculations, we take $p_{\perp}^c = 3\sqrt{\epsilon_y}I_{pn}^{-1/4}$ as the maximal transverse momentum of the tunneled electron (other fast electrons with momentum larger than p_{\perp}^c , only constituting $\approx 0.0004\%$ of the whole electron ensemble, are too rare to be considered), therefore if $p_{\perp}^c < p_{\text{drift}}$ then one can assert that all the electrons can not return and no shepherd electron effect would be observed. With the above consideration, we can obtain a criterion

$$I_{pn} = n^{2/5}(\epsilon/6\omega)^{-4/5}, \quad (4)$$

fitting the ionization potentials of the Rb atom³³, i.e., $I_{p1} = 4.18$ eV, $I_{p2} = 27.29$ eV, $I_{p3} = 39.25$ eV, $I_{p4} = 50.20$ eV, $I_{p5} = 68.44$ eV, $I_{p6} = 82.90$ eV, and $I_{p7} = 98.67$ eV. To this end, we add the electrons one by one, and the system energy is minimized at each step and fitted to the experimental values. This gives rise to the atomic parameters $\xi_1 = 2.5053$, $\xi_2 = 2.4784$, $\xi_3 = 2.4413$, $\xi_4 = 2.4216$, $\xi_5 = 2.3205$, $\xi_6 = 2.2707$, and $\xi_7 = 2.4520$. Correspondingly, the distances from the electrons to the nucleus are $r_1 = 5.77$, $r_2 = 1.43$, $r_3 = 1.29$, $r_4 = 1.24$, $r_5 = 1.02$, $r_6 = 0.94$, and $r_7 = 1.33$. The electron configuration is demonstrated in Fig. 1a, which highly resembles the shell structure of a Rb atom. We further apply random Euler rotations

$$A = \begin{bmatrix} -S\varphi S\eta + C\varphi C\theta C\eta & -S\varphi C\eta - C\varphi C\theta S\eta & C\varphi S\theta \\ C\varphi S\eta + S\varphi C\theta C\eta & C\varphi C\eta - S\varphi C\theta S\eta & S\varphi S\theta \\ -S\theta C\eta & S\theta S\eta & C\theta \end{bmatrix} \quad (6)$$

to the above configuration to obtain an ensemble of electrons with varying initial positions and momenta, which is implemented by the Monte Carlo sampling technique. Here, φ , η , and θ ($0 \leq \varphi \leq 2\pi$, $0 \leq \eta \leq 2\pi$, $-1 \leq \cos \theta \leq 1$) are the Euler angles while S and C represent the sine and cosine functions, respectively. In practice, considering the symmetry of the Hamiltonian H_0 , all electrons' position vectors are rotated with the same Euler angles and the momentum of each electron is rotated independently.

Having created a micro-canonical ensemble of classical atoms, we then exploit the CTMC-H model to simulate the dynamics of the laser-driven Rb system $H = H_0 + \sum_{i=1}^N \mathcal{E}(t) \cdot \mathbf{r}_i$ by solving the canonical equations $d\mathbf{r}_i/dt = \partial H/\partial \mathbf{p}_i$, $d\mathbf{p}_i/dt = -\partial H/\partial \mathbf{r}_i$ numerically with the standard 4–5th Runge-Kutta algorithm. The ionization events are identified according to the final energies of the electrons. For a given laser parameter, more than 10^6 classical trajectories are traced to ensure the convergence of the statistical results. After running a large ensemble of trajectories, ionization probabilities \mathcal{P}_n are calculated as $\mathcal{P}_n = \Xi_n/\Xi_{\text{tot}}$, where Ξ_n is the number of ionization events ending up with the final charge state Rb^{n+} and Ξ_{tot} is the total number of trajectories simulated⁶². The ion momentum spectra shown in Fig. 3 are obtained from the final momentum vectors of the ionized electrons according to the momentum conservation law.

Before closing this section, we would like to make some additional remarks regarding the CTMC-H model utilized in our simulations. Firstly, there are various procedures for preparing the classical trajectory ensembles (see, e.g., refs. 63,64), in which the distances from the electrons to the core are not fixed and can vary. However, the procedure by Abrines and Percival⁶³ is more suitable for a single-electron system but might suffer from unphysical autoionization (ionization even without the laser field) when extended to multi-electron situations. On the other hand, the pilot model⁶⁴ can partially alleviate the unphysical autoionization problem due to the soft-core parameter adopted for the core potential. Yet it is restricted to two- or three-electron systems. Therefore neither of these methods can be applied to the current studies on NSMI of Rb, which involves up to seven electrons. In the current CTMC-H model, the radii of the electrons are fixed which correspond to the stable points of the phase space, and thus can effectively prevent the unphysical autoionization without a laser field. Furthermore, the Heisenberg potential is more flexible in optimizing the ionization energies of the electrons, which is crucial for obtaining the expected atomic shell structure and reasonable ionization cross-sections⁶¹.

Secondly, this paper aims at demonstrating some intriguing phenomena due to the concept of shepherd electron. We note that a recent paper has shown that the specific form of the potential may quantitatively influence both the ionization yield and the ion momentum distribution⁶⁵. Nevertheless, in the section of Phase Diagram, our analytical theory that does not rely on the specific form

of the ionic potential seems to explain the numerical results very well, which suggests that the general pictures of shepherd electron are not sensitive to the exact form of the core potential. Looking forward, it would be interesting to quantitatively compare the results predicted by different models in a future study.

Data availability

The data that support the findings of this study are available from the corresponding author upon reasonable request.

Code availability

The code that support the findings of this study are available from the corresponding author upon reasonable request.

Received: 22 May 2023; Accepted: 13 September 2023;

Published online: 04 October 2023

References

- Eckle, P. et al. Attosecond angular streaking. *Nat. Phys.* **4**, 565 (2008).
- Pfeiffer, A. N., Cirelli, C., SmolarSKI, M., Dörner, R. & Keller, U. Timing the release in sequential double ionization. *Nat. Phys.* **7**, 428 (2011).
- Corkum, P. B. Plasma perspective on strong-field multiphoton ionization. *Phys. Rev. Lett.* **71**, 1994 (1993).
- Becker, W., Liu, X. J., Ho, P. J. & Eberly, J. H. Theories of photoelectron correlation in laser-driven multiple atomic ionization. *Rev. Mod. Phys.* **84**, 1011 (2012).
- Weber, T. H. et al. Correlated electron emission in multiphoton double ionization. *Nature* **405**, 658 (2000).
- Staudte, A. et al. Binary and Recoil Collisions in Strong Field Double Ionization of Helium. *Phys. Rev. Lett.* **99**, 263002 (2007).
- Rudenko, A. et al. Correlated Two-Electron Momentum Spectra for Strong-Field Nonsequential Double Ionization of He at 800 nm. *Phys. Rev. Lett.* **99**, 263003 (2007).
- Liu, Y. Q. et al. Strong-Field Double Ionization of Ar below the Recollision Threshold. *Phys. Rev. Lett.* **101**, 053001 (2008).
- Liu, Y. Q. et al. Multiphoton Double Ionization of Ar and Ne Close to Threshold. *Phys. Rev. Lett.* **104**, 173002 (2010).
- Haan, S. L., Van Dyke, J. S. & Smith, Z. S. Recollision Excitation, Electron Correlation, and the Production of High-Momentum Electrons in Double Ionization. *Phys. Rev. Lett.* **101**, 113001 (2008).
- Ye, D. F., Liu, X. & Liu, J. Classical trajectory diagnosis of a fingerlike pattern in the correlated electron momentum distribution in strong field double ionization of helium. *Phys. Rev. Lett.* **101**, 233003 (2008).
- Ye, D. F. et al. Scaling Laws of the Two-Electron Sum-Energy Spectrum in Strong-Field Double Ionization. *Phys. Rev. Lett.* **115**, 123001 (2015).
- Katsoulis, G. P., Hadjipittas, A., Bergues, B., Kling, M. F. & Emmanouilidou, A. Slingshot Nonsequential Double Ionization as a Gate to Anticorrelated Two-Electron Escape. *Phys. Rev. Lett.* **121**, 263203 (2018).
- Parker, J. S. et al. High-Energy Cutoff in the Spectrum of Strong-Field Nonsequential Double Ionization. *Phys. Rev. Lett.* **96**, 133001 (2006).
- Chen, Z. J., Liang, Y. Q. & Lin, C. D. Quantum Theory of Recollisional ($e, 2e$) Process in Strong Field Nonsequential Double Ionization of Helium. *Phys. Rev. Lett.* **104**, 253201 (2010).
- Hao, X. L. et al. Quantum Effects in Double Ionization of Argon below the Threshold Intensity. *Phys. Rev. Lett.* **112**, 073002 (2014).
- Maxwell, A. S. & Figueira de Morisson Faria, C. Controlling Below-Threshold Nonsequential Double Ionization via Quantum Interference. *Phys. Rev. Lett.* **116**, 143001 (2016).
- Walker, B. et al. Double ionization in the perturbative and tunneling regimes. *Phys. Rev. A* **48**, R894 (1993).
- Gillen, G. D., Walker, M. A. & VanWoerkom, L. D. Enhanced double ionization with circularly polarized light. *Phys. Rev. A* **64**, 043413 (2001); Guo, C., & Gibson, G. N. Ellipticity effects on single and double ionization of diatomic molecules in strong laser fields. *Phys. Rev. A* **63**, 040701(R) (2001).
- Wang, X. & Eberly, J. H. Elliptical polarization and probability of double ionization. *Phys. Rev. Lett.* **105**, 083001 (2010).
- Mauger, F., Chandre, C. & Uzer, T. Recollisions and correlated double ionization with circularly polarized light. *Phys. Rev. Lett.* **105**, 083002 (2010).
- Fu, L. B., Xin, G. G., Ye, D. F. & Liu, J. Recollision dynamics and phase diagram for nonsequential double ionization with circularly polarized laser fields. *Phys. Rev. Lett.* **108**, 103601 (2012).

23. Dubois, J., Chandre, C. & Uzer, T. Envelope-driven recollisions triggered by an elliptically polarized pulse. *Phys. Rev. Lett.* **124**, 253203 (2020).
24. Yamakawa, K. et al. Many-electron dynamics of a Xe atom in strong and superstrong laser fields. *Phys. Rev. Lett.* **92**, 123001 (2004).
25. Rudenko, A. et al. Correlated multielectron dynamics in ultrafast laser pulse interactions with atoms. *Phys. Rev. Lett.* **93**, 253001 (2004).
26. Gubbini, E., Eichmann, U., Kalashnikov, M. & Sandner, W. Core relaxation in atomic ultrastrong laser field ionization. *Phys. Rev. Lett.* **94**, 053602 (2005).
27. Palaniyappan, S. et al. Ultrastrong field Ionization of Ne^{n+} ($n \leq 8$): rescattering and the role of the magnetic field. *Phys. Rev. Lett.* **94**, 243003 (2005).
28. Sorokin, A. A. et al. Photoelectric effect at ultrahigh intensities. *Phys. Rev. Lett.* **99**, 213002 (2007).
29. DiChiara, A. D. et al. Relativistic MeV photoelectrons from the single atom response of argon to a 10^{19} W/cm² laser field. *Phys. Rev. Lett.* **101**, 173002 (2008).
30. Wessels, P. et al. Absolute strong-field ionization probabilities of ultracold rubidium atoms. *Commun. Phys.* **1**, 32 (2018).
31. De Silva, A. H. N. C. et al. Using circular dichroism to control energy transfer in multiphoton ionization. *Phys. Rev. Lett.* **126**, 023201 (2021).
32. Zhu, G. et al. Controlling two-electron threshold dynamics in double photoionization of lithium by initial-state preparation. *Phys. Rev. Lett.* **103**, 103008 (2009).
33. Yuan, J. Y. et al. Ellipticity-dependent sequential over-barrier ionization of cold rubidium. *Phys. Rev. A* **102**, 043112 (2020).
34. In analogy to the celestial phenomena of shepherd satellites that herd the planetary ring of Saturn, see, e.g., Fridman, A. M., & Gorkavyy, N. N. *Physics Of Planetary Rings: Celestial Mechanics Of Continuous Media* (Springer, New York, 1999); Zeilik, M. *Astronomy: The Evolving Universe* (Cambridge University Press, 2002); Kalinski, M., & Eberly, J. H. New states of hydrogen in a circularly polarized electromagnetic field. *Phys. Rev. Lett.* **77**, 2420 (1996).
35. Ludlow, A. D., Boyd, M. M., Ye, J., Peik, E. & Schmidt, P. O. Optical atomic clocks. *Rev. Mod. Phys.* **87**, 637 (2015).
36. Anderson, M. H., Ensher, J. R., Matthews, M. R., Wieman, C. E. & Cornell, E. A. Observation of Bose-Einstein condensation in a dilute atomic vapor. *Science* **269**, 198 (1995).
37. Kirschbaum, C. L. & Wilets, L. Classical many-body model for atomic collisions incorporating the Heisenberg and Pauli principles. *Phys. Rev. A* **21**, 834 (1980).
38. Cohen, J. S. Extension of quasiclassical effective Hamiltonian structure of atoms through $Z=94$. *Phys. Rev. A* **57**, 4964 (1998).
39. Zhou, Y., Huang, C., Liao, Q. & Lu, P. Classical simulations including electron correlations for sequential double ionization. *Phys. Rev. Lett.* **109**, 053004 (2012).
40. Lötstedt, E., Kato, T. & Yamanouchi, K. Classical dynamics of laser-driven D_3^+ . *Phys. Rev. Lett.* **106**, 203001 (2011).
41. Zajfman, D. & Maor, D. "Heisenberg core" in classical-trajectory monte carlo calculations of ionization and charge exchange. *Phys. Rev. Lett.* **56**, 320 (1986).
42. Liu, S. W., Ye, D. F. & Liu, J. Fragmentation dynamics of positron-impact hydrogen ionization at near-threshold energies. *Phys. Rev. A* **101**, 052704 (2020).
43. Liu, S. W., Ye, D. F. & Liu, J. Classical simulation of spin-tagged collisional ionization at near-threshold energies. *J. Phys. B: Mol. Opt. Phys.* **53**, 145005 (2020).
44. Laroche, S., Talebpoory, A. & Chin, S. L. Non-sequential multiple ionization of rare gas atoms in a Ti:Sapphire laser field. *J. Phys. B: Mol. Opt. Phys.* **31**, 1201 (1998).
45. Landau, L. D., & Lifshitz, E. M. *Mechanics*, 3rd ed. (Pergamon Press, London, 1976).
46. Walker, B. et al. Precision measurement of strong field double ionization of helium. *Phys. Rev. Lett.* **73**, 1227 (1994).
47. Brabec, T., Ivanov, M. Y. & Corkum, P. B. Coulomb focusing in intense field atomic processes. *Phys. Rev. A* **54**, R2551 (1996).
48. Nubbemeyer, T., Gorling, K., Saenz, A., Eichmann, U. & Sandner, W. Strong-field tunneling without ionization. *Phys. Rev. Lett.* **101**, 233001 (2008).
49. Wu, J. et al. Multiple recapture of electrons in multiple ionization of the argon dimer by a strong laser field. *Phys. Rev. Lett.* **107**, 043003 (2011).
50. Augst, S., Strickland, D., Meyerhofer, D. D., Chin, S. L. & Eberly, J. H. Tunneling ionization of noble gases in a high-intensity laser field. *Phys. Rev. Lett.* **63**, 2212 (1989).
51. Ho, P. J., Panfili, R., Haan, S. L. & Eberly, J. H. Nonsequential double ionization as a completely classical photoelectric effect. *Phys. Rev. Lett.* **94**, 093002 (2005).
52. Young, L. et al. Femtosecond electronic response of atoms to ultra-intense X-rays. *Nature* **466**, 56 (2010).
53. Delone, N. B. & Krainov, V. P. Energy and angular electron spectra for the tunnel ionization of atoms by strong low-frequency radiation. *J. Opt. Soc. Am. B* **8**, 1207 (1991).
54. Wang, X. & Eberly, J. H. Effects of elliptical polarization on strong-field short-pulse double ionization. *Phys. Rev. Lett.* **103**, 103007 (2009).
55. Bryan, W. A. et al. Atomic excitation during recollision-free ultrafast multi-electron tunnel ionization. *Nat. Phys.* **2**, 379 (2006).
56. Brédy, R., Nguyen, H., Camp, H., Fléchar, X. & DePaola, B. D. MOTRIMS as a generalized probe of AMO processes. *Nucl. Instrum. Methods Phys. Res. B* **205**, 191 (2003).
57. Colgan, J., Pindzola, M. S. & Robicheaux, F. Lattice calculations of the photoionization of Li. *Phys. Rev. Lett.* **93**, 053201 (2004).
58. Thiede, J. H., Eckhardt, B., Efimov, D. K., Prauzner-Bechcicki, J. S. & Zakrzewski, J. Ab initio study of time-dependent dynamics in strong-field triple ionization. *Phys. Rev. A* **98**, 031401(R) (2018).
59. Ho, P. J. & Eberly, J. H. In-plane theory of nonsequential triple ionization. *Phys. Rev. Lett.* **97**, 083001 (2006).
60. Jiang, H. & He, F. Semiclassical study of nonsequential triple ionization of Ar in strong laser fields. *Phys. Rev. A* **104**, 023113 (2021).
61. Zhou, J. & Wang, X. Classical multielectron model atoms with optimized ionization energies. *Opt. Express* **30**, 16802 (2022).
62. Liu, J. *Classical Trajectory Perspective Of Atomic Ionization In Strong Laser Fields: Semiclassical Modeling* (Springer, New York, 2013).
63. Abrines, R. & Percival, I. C. Classical theory of charge transfer and ionization of hydrogen atoms by protons. *Proc. Phys. Soc.* **88**, 861 (1966).
64. Panfili, R., Haan, S. L. & Eberly, J. H. Slow-Down Collisions and Nonsequential Double Ionization in Classical Simulations. *Phys. Rev. Lett.* **89**, 113001 (2002).
65. Emmanouilidou, A., Peters, M. B. & Katsoulis, G. P. Singularity in the electron-core potential as a gateway to accurate multielectron ionization spectra in strongly driven atoms. *Phys. Rev. A* **107**, L041101 (2023).
66. Leopold, J. G. & Percival, I. C. Ionisation of highly excited atoms by electric fields III. Microwave ionisation and excitation. *J. Phys. B: Mol. Phys.* **12**, 709 (1979).

Acknowledgements

We are grateful to M. Weidemüller for valuable discussions. This work was supported by the National Natural Science Foundation of China (NSFC) (Grants No. 12174034, No. 12047510, No. 11827806, No. 11822401, and No. 11775030) and NSAF (Grants No. U2330401, No. U1930402, and No. U1930403).

Author contributions

S. L., D. Y., and Y. J. designed the research. S. L. and D. Y. performed the research and analyzed the data. S. L., D. Y., and J. L. prepared the paper. All authors discussed the results and the final version of the paper.

Competing interests

The authors declare no competing interests.

Additional information

Supplementary information The online version contains supplementary material available at <https://doi.org/10.1038/s42005-023-01392-w>.

Correspondence and requests for materials should be addressed to Difa Ye or Jie Liu.

Peer review information *Communications Physics* thanks Jakub Prauzner-Bechcicki and the other, anonymous, reviewer(s) for their contribution to the peer review of this work. A peer review file is available.

Reprints and permission information is available at <http://www.nature.com/reprints>

Publisher's note Springer Nature remains neutral with regard to jurisdictional claims in published maps and institutional affiliations.



Open Access This article is licensed under a Creative Commons Attribution 4.0 International License, which permits use, sharing, adaptation, distribution and reproduction in any medium or format, as long as you give appropriate credit to the original author(s) and the source, provide a link to the Creative Commons licence, and indicate if changes were made. The images or other third party material in this article are included in the article's Creative Commons licence, unless indicated otherwise in a credit line to the material. If material is not included in the article's Creative Commons licence and your intended use is not permitted by statutory regulation or exceeds the permitted use, you will need to obtain permission directly from the copyright holder. To view a copy of this licence, visit <http://creativecommons.org/licenses/by/4.0/>.

© The Author(s) 2023